Journal of Alloys and Compounds 688 (2016) 804–813

Contents lists available at ScienceDirect

Journal of Alloys and Compounds

journal homepage: http://www.elsevier.com/locate/jalcom

Biphasic Fe–Rh nanowires synthesized by AC electrodeposition

J.S. Riva [a, *], G. Pozo-López [a, b, c], A.M. Condó [a, d], M.S. Viqueira [a, b], S.E. Urreta [c], D.R. Cornejo [e], L.M. Fabietti [a, b, c]

[a] Consejo Nacional de Investigaciones Científicas y Técnicas (CONICET), Argentina
[b] Instituto de Física Enrique Gaviola, CONICET, Argentina
[c] Facultad de Matemática, Astronomía y Física, Universidad Nacional de Córdoba, Ciudad Universitaria, 5000 Córdoba, Argentina
[d] Centro Atómico Bariloche, Comisión Nacional de Energía Atómica, Instituto Balseiro, Universidad Nacional de Cuyo, Av. Bustillo 9500, 8400 San Carlos de Bariloche, Argentina
[e] Instituto de Física, Universidade de São Paulo, 05508-900 São Paulo, SP, Brazil

ARTICLE INFO

Article history:
Received 24 April 2016
Received in revised form
21 June 2016
Accepted 16 July 2016
Available online 27 July 2016

Keywords:
Fe–Rh polycrystalline nanowires
AC electrodeposition
Magnetization mechanism
Magnetoresistance

ABSTRACT

Fe and $Fe_{90}Rh_{10}$ (nominal) polycrystalline nanowire arrays, 20 nm in diameter and about 1–3 mm in length, are successfully synthesized by AC electrodeposition into the cylindrical pores of anodized aluminum oxide (AAO) nanotemplates. The effects of Rh addition to Fe nanowires on the resulting microstructure, magnetic hysteresis and magnetoresistance properties are explored. As deposited $Fe_{90}Rh_{10}$ nanowires are biphasic, with large α–Fe grains (>100 nm) and clusters of very small (1.7 nm) grains of the ClCs type α′-FeRh phase, with a composition near $Fe_{42}Rh_{58}$. Hysteresis loops as a function of the sample orientation relative to the external applied field indicate that the easy magnetization axis is parallel to the nanowire long axis at all temperatures. The coercive field decreases with rhodium addition, as expected for an effective uniaxial anisotropy controlled by shape effects; on contrary, the relative remanence (or squareness) slightly increases. The temperature dependence of the coercive field is consistent with a mechanism involving nucleation of inverse domains, with an apparent energy barrier at zero fields between 2.6 and 4.1 eV. Room temperature magnetoresistance in $Fe_{90}Rh_{10}$ arrays is negative and shows hysteresis at low fields. At low temperature a large hysteresis is observed for fields between the knees in the hysteresis loop, with field ranges of positive and negative magnetoresistance slopes, arising in domain wall nucleation and expansion to complete polarization reversal and in conventional anisotropic magnetoresistance, respectively.

1. Introduction

Nanomaterials consisting of magnetic metals and noble metals are essential in fields such as magnetic sensors, catalysts, optical detection and biomedical applications [1]. Magnetic metal elements (Fe, Co, Ni) have two 4*s* outer most electrons and an unsaturated 3*d* electron shell, which induce rich physicochemical properties, such as specific magnetic and catalytic performances [2,3]. Noble metals mainly contain 4*d* electrons (Ag, Ru, Rh, Pd) and 5*d* electrons (Au, Pt); compared with magnetic metals, noble metals have more profound electron structures, exhibiting insuperable advantages in the areas of catalysis and optical detection, based on the surface plasmon resonance (SPR) [4,5].

Magnetic catalysts have, in particular, the benefits of easy recovery and reuse after the completion; this not only obviates the requirement of catalyst filtration or centrifugation after the completion of reactions, but also provides a practical technique for recycling the magnetized nanostructured catalysts [6].

It is then of great scientific significance and applied value the design and development of new magnetic–noble metal multifunctional nanostructures, the exploration of their magnetic responses or catalytic activities and the study of the relationship between the observed properties and the size, component phases and microstructure of these bimetallic nanomaterials [7–12].

Bimetallic, one-dimensional nanostructures with high aspect ratios have been successfully developed; recent research works have focused mostly on nanowires of Fe–Pt and Co–Pt [13], Fe–Co [14,15], CoPd [16,17] and FePd [18]. On the contrary, the FeRh system has been investigated at the nanoscale in the case of core (Rh)-shell (Fe) Rh@Fe nanoparticles [1], but Fe–Rh nanowires have not

* Corresponding author.
E-mail address: jriva@famaf.unc.edu.ar (J.S. Riva).

http://dx.doi.org/10.1016/j.jallcom.2016.07.171
0925-8388/

yet been explored.

The main drawback of noble metals such as Rh is its high cost, so it is of prime importance to select an appropriate processing route to obtain the desired material, minimizing the number of synthesis steps and also looking for high performance with low Rh content. Regarding the processing route, the electrodeposition into templates has proven to be a relatively cheap and high yield technique for producing large nanowire arrays directly from the deposition procedure. In addition, the relationships between processing and microstructure and between the microstructure and those properties of interest must be established.

In this work, we focus on the synthesis of Fe-rich ($Fe_{90}Rh_{10}$) nanowires, and on the characterization of the resulting microstructure in the as-synthesized condition; size, morphology, phase composition and surface conditions are determined. The magnetic hysteresis and the electronic transport properties are also explored.

2. Experimental procedures

Fe and $Fe_{90}Rh_{10}$ nanowires were prepared by AC electrodeposition of the metallic ions into the pores of an anodized aluminum oxide (AAO) membrane. The porous alumina membranes were prepared via the conventional two step anodization process [19] applied to high-purity aluminum foils (99.995%). Before anodizing, the aluminum foils were degreased with acetone, electropolished in a H_2SO_4 + H_3PO_4 + H_2O 2:2:1 solution, and finally etched with NaOH to remove aluminum oxide from the surface. The foil was anodized under a constant voltage of 20 V in 0.3 M $H_2C_2O_3$ for 4 h at 276 K to form a layer of porous alumina. After the first anodizing step, the aluminum oxide film was dissolved in 0.20 M Cr_2O_3 and 0.40 M H_3PO_4 at 333 K for 1 h, to remove the oxide layer. The second anodizing step was carried out under the same conditions as the first one, for another 2 h. In these conditions, arrays of ordered pores 20 nm in diameter and about 3–4 μm in length were obtained, as shown in Fig. 1a. The membrane porosity P was estimated as $P = (\pi/2\sqrt{3})(D_p/D_{int})^2 = (0.10\pm0.01)$ [20], with $D_p = 20 \pm 2$ nm the pore diameter and $D_{int} = 60 \pm 4$ nm the mean centre-to-centre inter-pore distance in the array.

The electrodeposition of Fe nanowires was carried out in an aqueous electrolytic bath containing Fe ions, prepared with $FeSO_4$ $7H_2O$ 0.2 M, 0.009 M ascorbic acid (to avoid iron oxidation), and HBO 0.5 M, which was added to enhance conductivity. The pH value was adjusted to 5 by adding few drops of diluted H_2SO_4. The electrodeposition was conducted at room temperature under a sinusoidal wave of 200 Hz and 16 V_{rms}, for a few minutes.

$Fe_{90}Rh_{10}$ nanowires were then electrodeposited in an aqueous electrolytic bath with 0.10 M $FeSO_4 \cdot 7H_2O$, 0.0067 M $RhCl_3$, 0.75 g/L ascorbic acid and 30 g/L H_3BO_3 in ultrapure water (MilliQ RiOs 16, Millipore), maintaining the pH value at 4.0. Deposition was carried out at room temperature with an AC voltage of 15 V_{rms} and 60 Hz during 10 min. A two electrode electrochemical cell was used, where the aluminum still attached to the AAO template served as a working electrode and a graphite rod as an auxiliary one; oxygen was purged from the solutions by nitrogen bubbling before the experiments.

X-ray diffraction (XRD) was used to identify the phases in the nanowires; XRD profiles were recorded in a PANalytical Empyrean diffractometer, using Cu Kα radiation (λ = 1.5418 Å), in the 2θ range from 30° to 90°. The mean array composition was determined by energy-dispersive X-ray spectroscopy (EDS), in a JEOL JXA-8230 equipment, and the nanowire morphology was investigated in a scanning electron microscope (FE-SEM) Zeiss. Samples for XRD measurements were prepared by dissolving the remaining Al substrate in a $CuSO_4$ and HCl solution to eliminate intense Al X-ray peaks; samples for SEM observations were further immersed in a 1.0 M NaOH solution to dissolve the AAO template and separate the nanowires. After sonication and rinsing in distilled water, many dispersed nanowires were obtained, as illustrated in Fig. 1b.

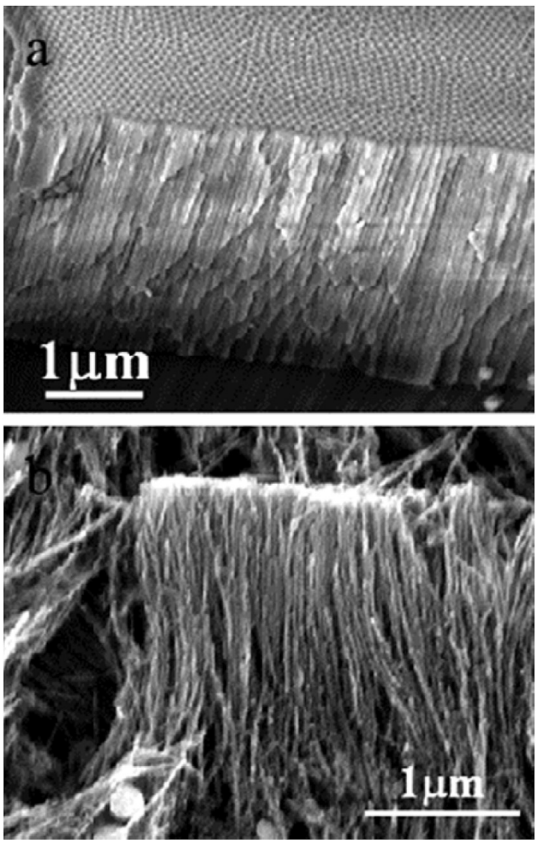

Fig. 1. SEM micrographs showing side views of (upper) an alumina template of 20 nm pore diameter and (bottom) of $Fe_{90}Rh_{10}$ nanowires, after dissolving the aluminum support and the alumina template.

The individual wire nanostructure and composition were investigated by transmission electron microscopy (TEM) in a Philips CM200UT microscope, operating at 200 kV, with an EDS analysis device. Samples for TEM observations were prepared by dispersing the liberated nanowires in ethanol and further depositing a drop of this emulsion on a holey carbon-coated copper grid.

Magnetic properties of Fe and $Fe_{90}Rh_{10}$ nanowires were measured in a vibrating sample magnetometer (VSM) Lakeshore 7300, at room temperature with a maximum field up to 1.5 T. Temperature dependence of magnetic properties was further explored in a commercial Magnetic Property Measurement System (MPMS Quantum Design), in the temperature range between 5 K and 300 K. The external field was applied parallel (PA) and perpendicular (PE) to nanowires. The total magnetic moment of the assembly has contributions from the Al support (paramagnetic), the alumina template (diamagnetic) and the metallic wires filling the pores (ferromagnetic), so the ferromagnetic component must be estimated after subtracting a linear contribution.

Electrical transport measurements were conducted in a commercial Physical Property Measurement System (PPMS Quantum Design), in the temperature range between 5 K and 300 K. Due to the limitations imposed by the sample geometry (see the inset in Fig. 10), four point resistance measurements could not be performed and only a two-probe measurement was feasible by bringing two copper wires with silver epoxy to a small area (typically 1 mm^2) on both sides of the AAO. Magnetoresistance was then measured in the longitudinal configuration, that is, with a magnetic

field $\mu_0\vec{H}$ between −9 T and 9 T, applied parallel to the current $\vec{I}$, flowing along the nanowire major axis. Owing to the high aspect ratio of these nanowires and that not all the wires are contacted, any spurious contact resistance is expected to be small compared to that of wires. When the resistance values are normalized to the value at a common temperature, the temperature dependences of this reduced resistance appears quite reproducible.

3. Results and discussion

3.1. Morphology and structure

As previously indicated, the mean composition of the Rh containing nanowire arrays was determined by EDS, after dissolving the remaining Al film and the alumina template; the mean value from three different regions in the sample resulted about $Fe_{90}Rh_{10}$; it is worth noting that this is a mean, nominal composition because the wires are not single-phase, as will be shown later.

Fig. 2 shows the X-ray diffraction profiles of the as-prepared Fe and $Fe_{90}Rh_{10}$ nanowires, without the aluminum support but still embedded (ordered) into the AAO template. The narrow peak at 2θ ~31.7° observed in both diffractograms corresponds to the polystyrene layer (PDF # 00-013-0836) deposited onto the alumina membranes to improve their mechanical resistance, and the peak at 43.7° corresponds to residual copper crystals.

Iron nanowires have a *bcc* cubic structure (PDF # 00-006-0696), with a preferred (110) orientation along the nanowires. In addition to the α-Fe diffraction lines, the $Fe_{90}Rh_{10}$ profile shows a broad peak at 42.7° which is indexed as the (110) peak of the ClCs-type α′-FeRh phase (ICSD # 108465). This identification was performed considering additional results (not shown) obtained from electron diffraction in the TEM in these samples, and also in another group of samples, with a higher Rh content ($Fe_{50}Rh_{50}$). In these new samples the faint diffraction rings hardly detected for the arrays with less Rh content are replaced by sharp and clear ones, corresponding to this ClCs-type phase.

The lattice constant values a_0 of the *bcc* iron phase present in the Fe and $Fe_{90}Rh_{10}$ nanowire arrays were obtained after fitting the most intense diffraction line (110) by a Pearson VII function, using the Win Fit! Beta Release 1.2.1 (June 97), Stefan Krumm. Institut für Geologie. Erlangen (Free software). The resulting values (a_{Fe} = 2.867 Å, a_{Fe90} = 2.864 Å) are quite similar and consistent, within experimental errors, with the crystalline structure of α-Fe (a = 2.866 Å, PDF # 00-006-0696).

The internal structure of Fe and $Fe_{90}Rh_{10}$ nanowires was further investigated with TEM techniques. Figs. 3–4 depict the results for Fe nanowires. They exhibit a branched shape, with a quite irregular surface, with a mean length of about (0.8 ± 0.1) μm and a diameter distribution that may be well fitted by a log-normal function, with median of 25.4 nm and σ = 0.22 (Fig. 3).

Selected area electron diffraction (SAED) patterns and EDS spectra confirm XRD results, in the sense that the wires mainly consist in a *bcc* Fe-rich phase; they are formed by quite large α-Fe grains, with longitudinal sizes between 100 and 1000 nm and lateral sizes similar to the wire diameter (Fig. 4a–b). An additional phase is also observed in the SAED patterns, as diffuse and faint rings, which can be identified as magnetite (Fe_3O_4). A detailed analysis of the wires indicates that they are coated by a (4 ± 1) nm thickness magnetite layer, formed by very small grains (<10 nm), as can be seen in Fig. 4d. This superficial oxide is likely to form during the subsequent baths applied during sample preparation for TEM, because the iron wire diameter is smaller but close to that of the template, while the final one is larger than this latter one. In that way, the mean wire diameter (including the oxide film) results in (26 ± 4) nm, according to the log-normal fit already presented in Fig. 3b, while the Fe nanowire diameter becomes (18 ± 2) nm. (see Table 1).

The morphology and structure of $Fe_{90}Rh_{10}$ nanowires are also explored by TEM, and the corresponding results are shown in Figs. 5 and 6. These nanowires are about (1.5 ± 0.3) μm long, and also show a branched profile, with a very small grained (4.4 nm mean size) magnetite film coating the surface (Fig. 6). The diameter distribution in the array was also fitted by a log-normal function with median = 27.2 nm and σ = 0.19, leading to a mean nanowire

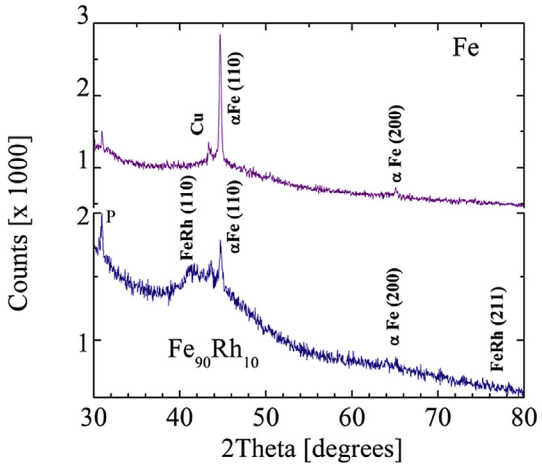

Fig. 2. XRD diagrams corresponding to Fe and $Fe_{90}Rh_{10}$ nanowire arrays after removal of the Al substrate. The reflection denoted by P arises from the polystyrene layer added to improve the membrane mechanical resistance. Residual Cu crystals, originated in the Al dissolution process, are also detected.

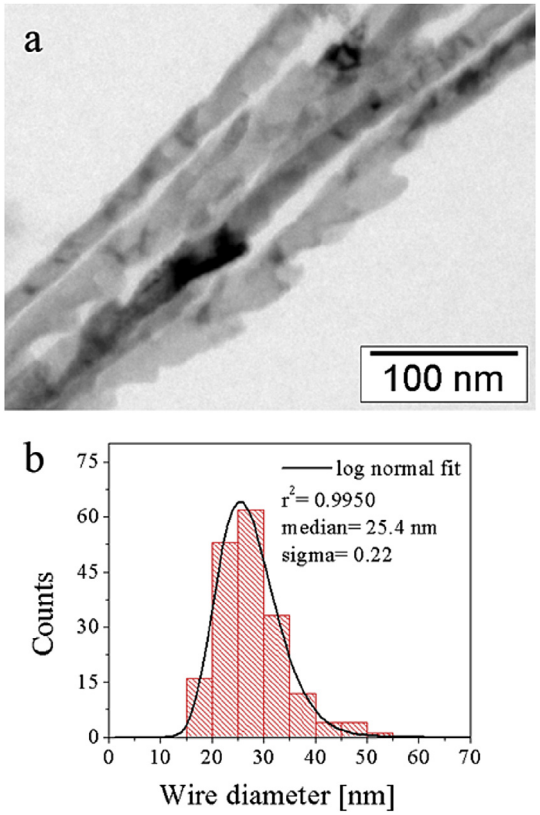

Fig. 3. (a) Bright field TEM micrograph of Fe nanowires, showing their branched and irregular shape. (b) Wire diameter histogram and its corresponding log-normal fit, resulting from TEM data.

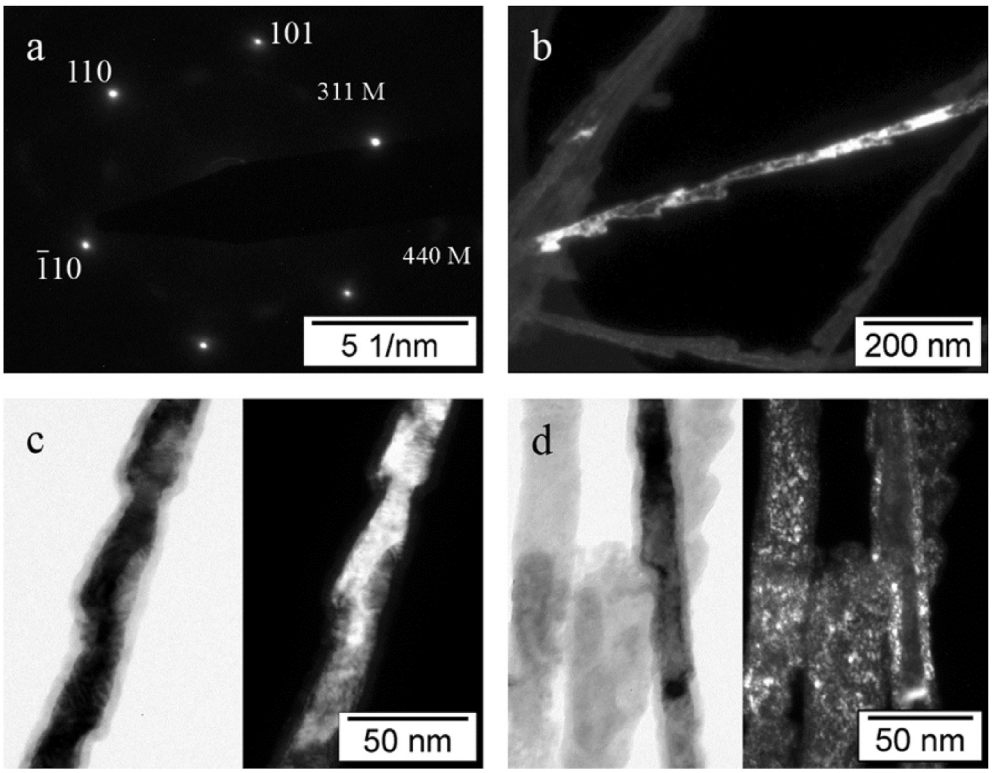

Fig. 4. (a) Electron diffraction [11] zone axis pattern corresponding to the α-Fe phase. Additional faint and diffuse spots are observed, which can be associated to magnetite (M) diffraction rings. (b) Dark field (DF) image with g = 110 showing a typical α-Fe grain. (c) Bright field (BF) image and corresponding dark field (DF) image with α-Fe g = 110 of a Fe nanowire. Wires are coated by a ~4 nm thickness magnetite layer. Bright field (BF) micrograph showing a group of Fe nanowires are shown in (d) with the corresponding dark field (DF) image with magnetite g = 311. The magnetite layer is composed of very small grains (<10 nm).

Table 1
Morphological parameters corresponding to the Fe and $Fe_{90}Rh_{10}$ nanowires. The mean grain size d_G, mean nanowire length L and diameter D corresponding to the different samples, and the estimated values of the demagnetizing nanowires' factors $N_{//}$ and $N_{\perp}$ [21] are listed. $Fe_3O_4^a$ and $Fe_3O_4^b$ correspond to the surface oxide film in Fe and FeRh wires, respectively. Values of the wire diameter without this outer magnetite coating are indicated between brackets.

Sample		Fe			$Fe_{90}Rh_{10}$
D [nm]		26 ± 4 (18 ± 2)			28 ± 4 (19 ± 1)
L [mm]		0.8 ± 0.1			3.0 ± 0.6
$N_{//}$		0.0105			0.0028
$N_{\perp//}$		0.4925			0.4986
Phases	α	$Fe_3O_4^a$	α	α′	$Fe_3O_4^b$
a_0 [nm]	0.2867 (1)	–	0.2864 (1)	0.307 (1)	–
d_G [nm]	150 ± 20	4.4 ± 0.2	140 ± 20	1.7 ± 0.4	4.4 ± 0.2

diameter of (28 ± 4) nm. The Fe-phase grain diameter is (20 ± 2) nm and the longitudinal size between 100 and 1000 nm.

At the tip of some nanowires and between large Fe rich grains, ensembles of very small grains of a Rh-rich ClCs-type phase are frequently observed. This Rh-rich phase has a composition (42 ± 5) at.% Fe − (58 ± 5) at.% Rh and is identified as the ordered $L2_1$ α′ phase of the Fe–Rh binary system [22,23]. The grain size distribution of this ordered Rh-rich phase was fitted by a log-normal function leading to a mean value of about (1.7 ± 0.5) nm

3.2. Room temperature magnetic properties

The room temperature hysteresis loops of as-prepared samples have been measured with the applied magnetic field parallel and perpendicular to the nanowire axis and they are depicted in Fig. 7, together with the same loops measured at 5 K. In both arrays the easy magnetization axis is always parallel to the major nanowire axis, as expected for the large shape anisotropy associated to high aspect ratios and Fe contents. The corresponding hysteresis parameters at 300 K and at 5 K are listed in Table 2.

The coercive field of these nanowire arrays may be described by the expression [24,25]:

$$\mu_0 H_C = \mu_0 \frac{2\,K_u}{J_s} - N_{eff} J_S \tag{1}$$

with K_u an effective uniaxial anisotropy and N_{eff} an effective demagnetizing factor, taking into account inter-wire interactions and other magnetostatic demagnetizing effects. This expression for the coercive field is consistent with different magnetization reversal mechanisms so additional measurements have to be considered to determine which of them is actually responsible for the observed coercivity. The coercive field dependence on the angle ϕ between the applied magnetic field and the long wire axis (easy magnetization axis) is closely related to the operating mechanism so it is further investigated at room temperature.

3.3. Magnetization mechanism

A possible mechanism controlling coercivity in polycrystalline Fe nanowire arrays, with relatively large grains, has been reported to be the nucleation by a process of local curling of inverse domains and their further expansion to sweep the entire grain [14]. Considering reversal in a small prolate spheroid (nucleus) with an effective uniaxial anisotropy K_u, given by contributions of crystalline and shape (related to the wire aspect ratio) anisotropies, the

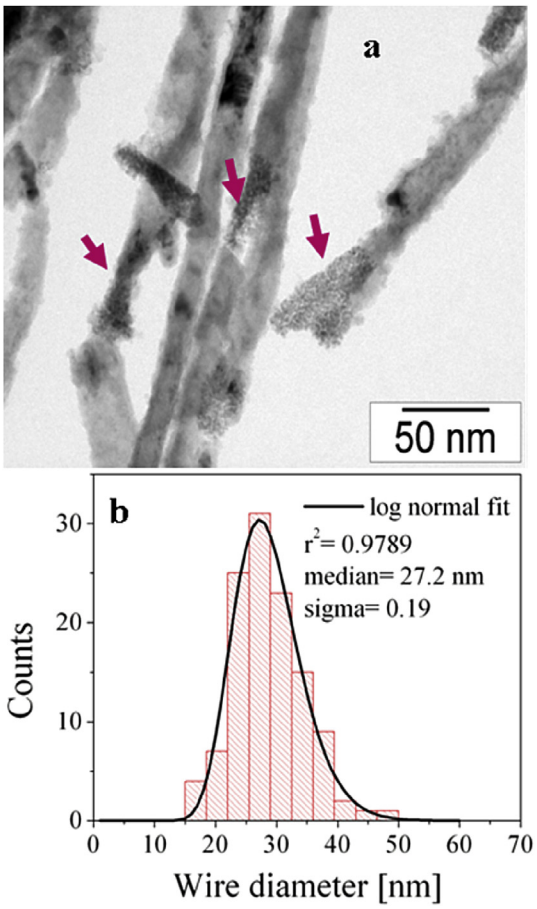

Fig. 5. (a) Bright field (BF) TEM micrograph of a group of $Fe_{90}Rh_{10}$ nanowires. Wires present a branched shape; at their tips and between α-Fe phase grains a new phase - indicated by arrows - is observed. (b) Wire diameter histogram and its corresponding log-normal fit, resulting from TEM data.

angular dependence of the nucleation field becomes [14,26]:

$$\mu_0 H_C(\phi) = \mu_0 \frac{2K_u}{J_s} \frac{\left(n_{\parallel} - s\right)(n_{\perp} - s)}{\sqrt{\left(n_{\parallel} - s\right)^2 sin^2\phi + (n_{\perp} - s)^2 cos^2\phi}} - N_{eff} J_S. \quad (2)$$

Here, $L_x = \sqrt{2A\mu_0/J_S^2}$ is the exchange length, which is composition sensitive through J_S values, A is the exchange energy constant, $R = D/2$ is the mean wire radius and $s = k L_x^2/R^2$, with $k = 1.2049$ [27], takes values of 0.0482 and 0.0583 for Fe and $Fe_{90}Rh_{10}$ arrays, respectively. Parameters $n_{\parallel}$ and $n_{\perp} = (1 - n_{\parallel})/2$ are the nucleus effective demagnetizing factors. Finally, the second term in the right hand of equation (2) is a mean value of the dipolar interaction field for applied fields forming angles between 0 and $\pi/2$ with the major wire axis.

The angular variation of the coercive field and the relative remanence S in the arrays are shown in Fig. 8. The main feature observed is that coercivity and squareness remain high up to higher angles in the Rh containing array, as if an effective "easy cone" of about $\pi/6$ were developed. The solid line in Fig. 8a is the best fit of equation (2) to the experimental data and the resulting parameters' values are listed in Table 3. The effective demagnetizing factor N_{eff} and the uniaxial anisotropy constant K_u are larger in the Fe array than in the $Fe_{90}Rh_{10}$ one, as expected for a system with predominant shape anisotropy and large local magnetostatic effects. An upper bound for the shape anisotropy constant is given by $K_{shape} \cong 1/4 J_S^2/\mu_0$ leading to values of 9.2 × 10^5 J/m^3 and 7.45 × 10^5 J/m^3 for Fe and $Fe_{90}Rh_{10}$ arrays, in good agreement with the fitted values of K_u, listed in Table 3. These facts confirm than the leading contribution to the effective anisotropy still arises from magnetostatic shape effects; however, as pointed out before, in the Rh containing arrays coercivity and squareness are less sensitive to departures from the easy axis direction of the individual nanowires, up to nearly $\phi = 30°$, as if local magnetostatic demagnetizing fields at the nucleation sites were less intense and more isotropic.

3.4. Temperature dependent hysteresis properties

The temperature dependence of the coercive field and the loop squareness S (=Jr/Js) are shown in Fig. 9 and the data for T = 5 K and T = 300 are included in Table 2. It is observed that the coercivity reduces with Rh addition from 0.192 T to 0.175 T (~10%) at room temperature certainly due to the reduction in the shape anisotropy by replacing Fe atoms by non magnetic Rh atoms; in both systems coercivity gradually increases when temperature decreases to 5 K, 28% in $Fe_{90}Rh_{10}$ and 39% in Fe nanowires.

The squareness is always higher in samples $Fe_{90}Rh_{10}$, and this is almost constant in the temperature range studied. Squareness takes very small values (less than 0.1) in the case of hysteresis loops under fields applied perpendicular to the nanowires.

Assuming a thermally activated, nucleation controlled magnetization reversal mechanism, the temperature and field dependence of the apparent activation energy barrier E and the coercive field $\mu_0 H_C$ may be described as [28]:

$$E = E_0 \left(1 - \frac{H}{H_0}\right), \quad (3)$$

Then, the applied field for $J = 0$ becomes:

$$\mu_0 H_C = \mu_0 H_0 - \left[\frac{\mu_0 H_0 25\, k_B}{E_0}\right] T \quad (4)$$

where E_0 and $\mu_0 H_0$ are respectively, the apparent activation barrier height and the critical field for reversal, both at T = 0 K. The resulting values for these parameters are listed in Table 4. The activation energy values are comparable to those reported by Paulus et al. [29] for a mechanism of inverse domain nucleation in Fe nanowires (2.4–5.1 eV). The apparent activation energy barrier is larger in $Fe_{90}Rh_{10}$ nanowires than in the Fe ones indicating that more energy is necessary to create a domain wall in the nucleation sites. An increased domain wall energy density may be expected for sites in the α′-FeRh phase, with a magnetocrystalline energy of about 1.3 × 10^5 J/m^3. [30], higher than that of α-Fe (0.48 × 10^5 J/m^3), but large random anisotropy effects are also expected in this very small grained phase, which largely reduce the effective anisotropy. Another factor affecting the zero field and temperature barrier, is the magnitude of magnetostatic stray fields, which are expected to be smaller in nucleation sites at the α-α′ interfaces. The apparent activation barrier in the perpendicular configuration is larger in both array types; this fact may be related to an also larger difference between the applied field (the ordinate in plots shown in Fig. 9) and the local actual internal field for the perpendicular geometry.

3.5. Electrical behavior

The zero field electrical resistance of each array composition was measured between 4 K and 300 K, at a heating rate of 2 K/min, and

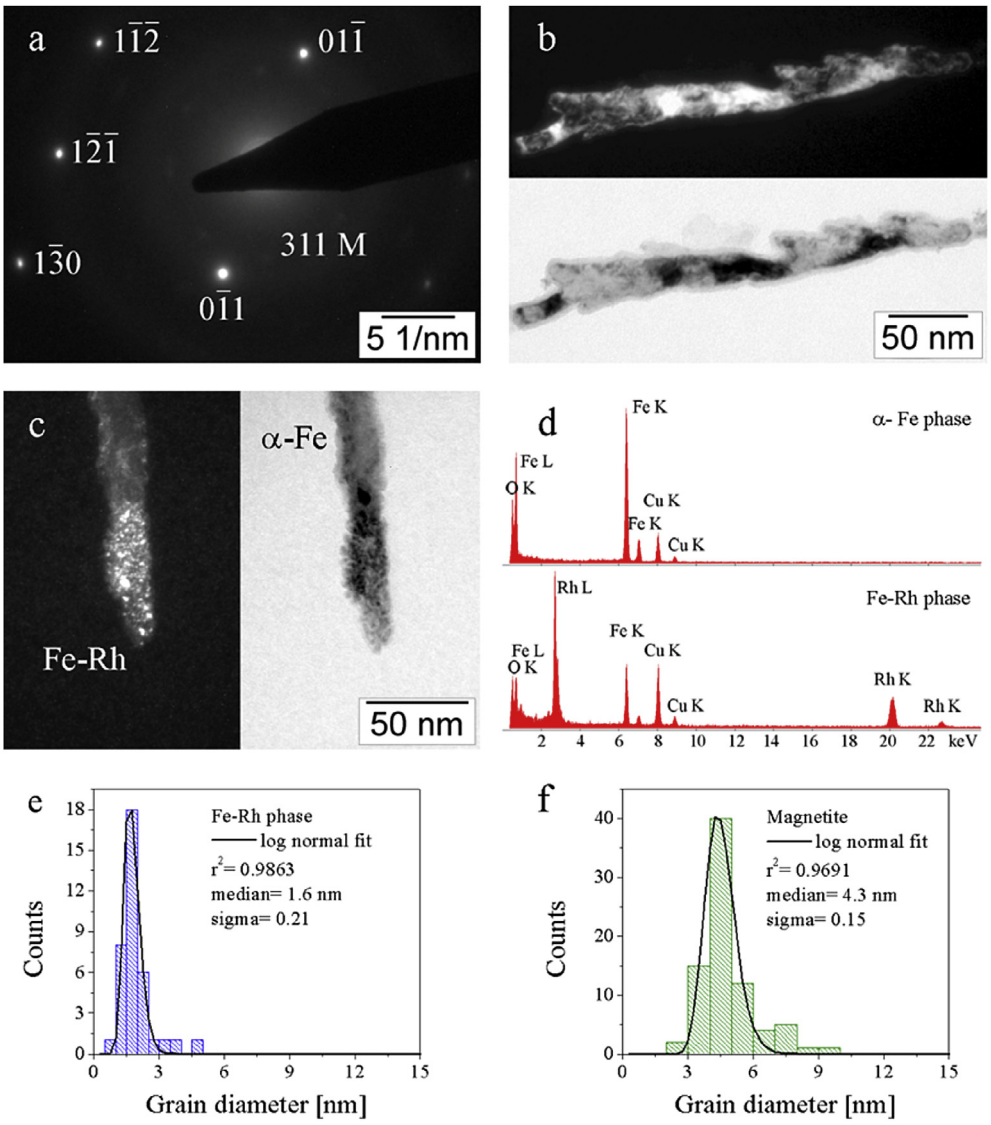

Fig. 6. (a) Electron diffraction [311] zone axis pattern corresponding to the α-Fe phase. Additional faint and diffuse spots are observed, which can be associated to magnetite (M) diffraction rings. (b) Bright field (BF) micrograph and the corresponding dark field (DF) image with α-Fe g = 110 of a $Fe_{90}Rh_{10}$ nanowire. A ~4 nm thick magnetite layer is observed at the wire surface. (c) Bright field (BF) micrograph of a $Fe_{90}Rh_{10}$ nanowire and the corresponding dark field (DF) image with Fe–Rh ClCs-structure type g = 110. (d) EDS spectra of the α-Fe phase and the Fe–Rh phase grown in the nanowire. Cu lines arise from the TEM grid. (e) Magnetite grain size histogram and its corresponding log-normal fit, resulting from TEM data. (f) Fe–Rh phase grain size histogram and its corresponding log-normal fit, resulting from TEM data.

representative curves are displayed in Fig. 10. They both exhibit the expected metallic behavior; similar mean values of the temperature resistance coefficient (TRC) are found in the mentioned temperature range, about $(14 \pm 6)\ 10^{-4}\ K^{-1}$ and $(12 \pm 5)\ 10^{-4}\ K^{-1}$ for Fe and $Fe_{90}Rh_{10}$ samples, respectively. These effective TRC values are smaller than those reported for bulk iron near room temperature ($62\ 10^{-4}\ K^{-1}$, [31]) and also for rhodium ($43\ 10^{-4}\ K^{-1}$ [32]). When $T \rightarrow 0$, the resistance curve goes through a shallow minimum, at about 16 K for Fe and 13 K for $Fe_{90}Rh_{10}$ arrays, both during heating and cooling (not shown). It is not clear at present if this deviation from the Matthiessen's rule arises from the two-current character of the conduction [33] or any other phenomenon.

Resistivity measurements as a function of the applied field provide microscopic information on the alignment of the magnetic moments on the length scale of the electronic mean free path. With this aim, the effect of a longitudinal magnetic field on the $Fe_{90}Rh_{10}$ array resistance was investigated and the results are summarized in Fig. 11, for the electric current flowing along the wires and the magnetic field also applied parallel the wires.

Magnetoresistance effects in bulk iron single- [34–36] and polycrystals [37,38], and also in Fe whiskers [39] have been investigated in the range between 300 K and 4.2 K and in fields up to 50 kOe. At 300 K the magnetoresistance shows an initial positive region connected with the irreversible magnetization process, while at high fields it shifts to a negative slope. At low temperatures, the low-field longitudinal magnetoresistance becomes negative and at 4.2 K the longitudinal magnetoresistance reaches minimum values at 400–1000 Oe.

Large and constant values of electrical resistance are obtained for the unfilled alumina membrane, with both the sputtered Au layer and built up contacts, for fields up to 9 T, so the measured values for the filled membranes are due to the metallic nanowires. At 300 K, when the field is applied parallel to the current, the magnetoresistance of the filled $Fe_{90}Rh_{10}$ nanowire array undergoes a negative variation superimposed to a drift during measurement, which makes difficult any precise determination. The upper curve

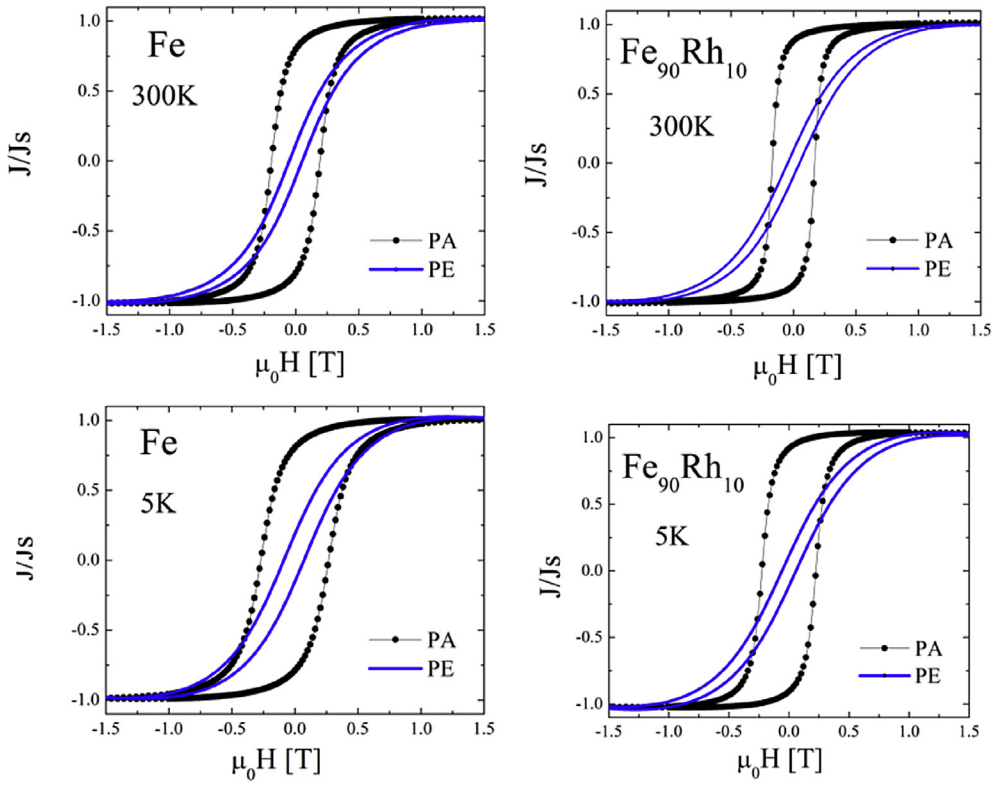

Fig. 7. Magnetic hysteresis loops of Fe and $Fe_{90}Rh_{10}$ nanowires, measured with the applied field parallel (PA) and perpendicular (PE) to the nanowire major axis.

Table 2
Coercive fields μ_0H_C(PA), μ_0H_C(PE) and squareness factors [$S = J_R/J_S$] S(PA) and S(PE), as determined with the applied field parallel (PA) and perpendicular (PE) to the major wire axis, at 300 K and 5 K.

Sample	T [K]	μ_0H_C(PA) [T]	μ_0H_C(PE) [T]	S (PA)	S (PE)	J_S [T]	$K_1 \times 10^5$ [Jm^{-3}]
Fe	5	0.2686	0.0789	0.72	0.11		0.57
	300	0.1922	0.0483	0.73	0.08	2.16	0.48
$Fe_{90}Rh_{10}$	5	0.2248	0.0526	0.83	0.06		
	300	0.1751	0.0448	0.80	0.06	1.95	1.3

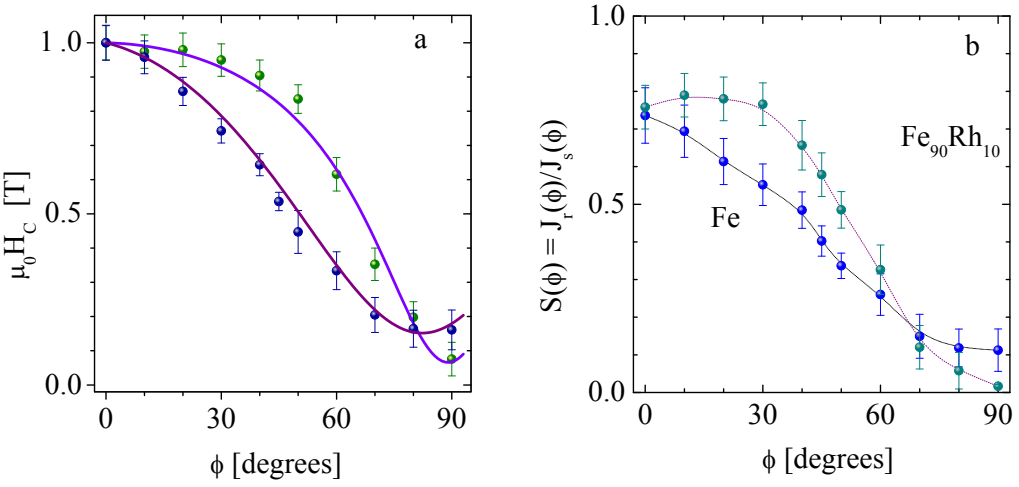

Fig. 8. Angular dependence of the coercive field (a) and squarness (b) for the nanowire arrays investigated; ϕ is the angle between the applied magnetic field and the long wire axis. Solid lines in (a) are best fits of Equation (2) to the experimental data; main fitted parameter values are quoted in Table 3.

in Fig. 11a illustrates this effect in the field range of ±9 T, while that at the bottom shows the range up to 2 T, where a negative magnetoresistance is observed.

The magnetoresistance of the same $Fe_{90}Rh_{10}$ sample array at

Table 3
The effective demagnetizing factors N_{eff}, the nucleus effective demagnetizing factors $n_\perp$ and $n_\parallel$, the shape $K_{sh}(= 1/2\mu_0(N_\perp - N_\parallel)J_S^2)$ and the effective uniaxial K_u anisotropies are given together with values of the exchange length $L_{ex}(= \sqrt{2A\mu_0/J_S^2})$.

Sample	K_u 10^5 [Jm^{-3}]	K_{sh} 10^5 [Jm^{-3}]	N_{eff}	$n_\parallel$	$n_\perp$	L_{ex} [nm]
Fe	8.2	9.2	0.20	0.420	0.247	2.0
$Fe_{90}Rh_{10}$	5.8	7.5	0.14	0.126	0.347	2.2

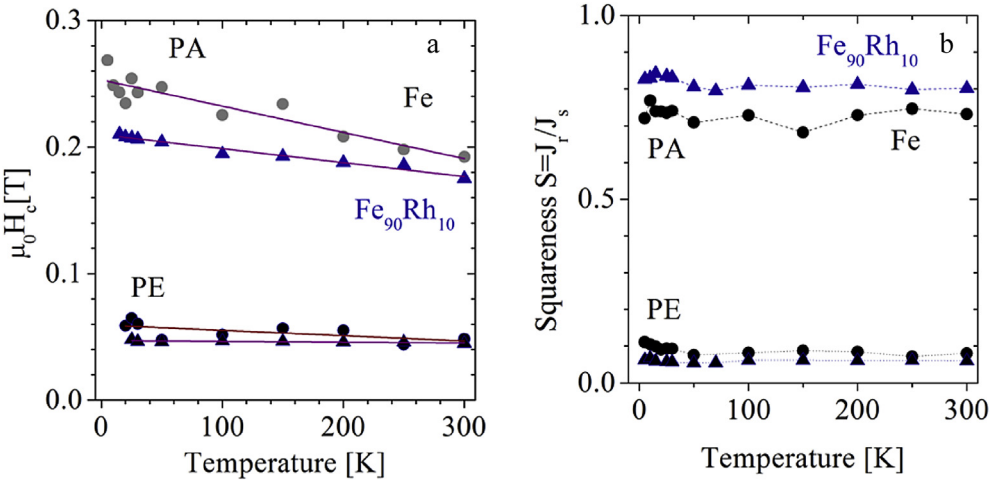

Fig. 9. Temperature dependence on the coercivity (a) and squareness (b), in Fe and $Fe_{90}Rh_{10}$ nanowires. PA and PE indicate that the magnitude is measured with the magnetic field applied parallel or perpendicular to the nanowire long axis. Lines in plot (a) are the best linear fits to Equation (4).

Table 4
Coercive field in absence of thermal activation $\mu_0 H_0$ and the apparent activation energy at zero applied field E_0. PA and PE indicate that the field is applied parallel or perpendicular to the long wire axis, respectively.

Sample	$\mu_0 H_{0PA}$ [mT]	$\mu_0 H_{0PE}$ [mT]	E_{0PA}		E_{0PE}	
			[kJ/mol]	[eV]	[kJ/mol]	[eV]
Fe	253 ± 4	59 ± 3	250 ± 10	2.6 ± 0.1	306 ± 10	3.1 ± 0.1
$Fe_{90}Rh_{10}$	210 ± 4	48 ± 3	396 ± 20	4.1 ± 0.1	553 ± 20	5.7 ± 0.1

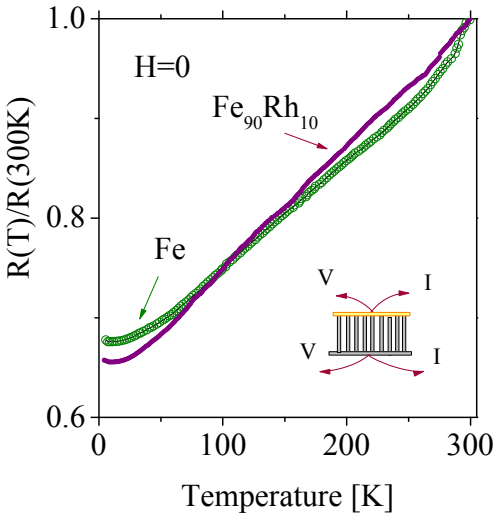

Fig. 10. Temperature dependence of the relative resistance in Fe and $Fe_{90}Rh_{10}$ nanowire arrays, as measured in a two probe configuration as illustrated in the inset.

10 K is shown in Fig. 11b, for an applied field between ±9 T. The low field magnetoresistance at this temperature is shown in Fig. 11c, together with the hysteresis loop displayed in Fig. 7 to illustrate the correlation between magnetization and magnetoresistance.

At low temperature, Fig. 11b, a different behavior is found when the applied field increases starting from remanence; first, resistance rapidly decreases and after a sharp minimum, it increases again to a local maximum that is higher than the remanent value. Then, after going through this local maximum the magnetoresistance decreases almost linearly, goes through a second minimum and finally increases monotonously with the applied field (~B^2), in a regime mostly controlled by Lorentz Magnetoresistance (LMR). By further decreasing the magnetic field, the resistance first decreases reversibly down to about 2 T and then, it reduces until remanence exhibiting hysteresis.

From Fig. 11c it may be observed that longitudinal magnetoresistance exhibits hysteresis mainly within the field range where a large portion of nanowires in the array reverse their polarization, developing a net magnetization in the direction of the applied field; the decrease in resistance beyond the local maxima is then connected with the final magnetic moments reversible rotation towards the applied field. This can be understood in the framework of the anisotropic magnetoresistance (AMR) phenomenon related to the change in the orientation between magnetization and current. In addition, these results also suggest that a multidomain-like configuration should be present in these nanowires near zero fields, with the magnetization of these domains partially oriented along the normal to the wire. The magnetization reversal process initiates by the nucleation of a reversed domain; this first nucleation process is accompanied by a new domain nucleation in the neighboring region, activated by the change in stray field produced by the first domain nucleation. The domain nucleation "avalanche" continues until the whole magnetization of the wire has been reversed.

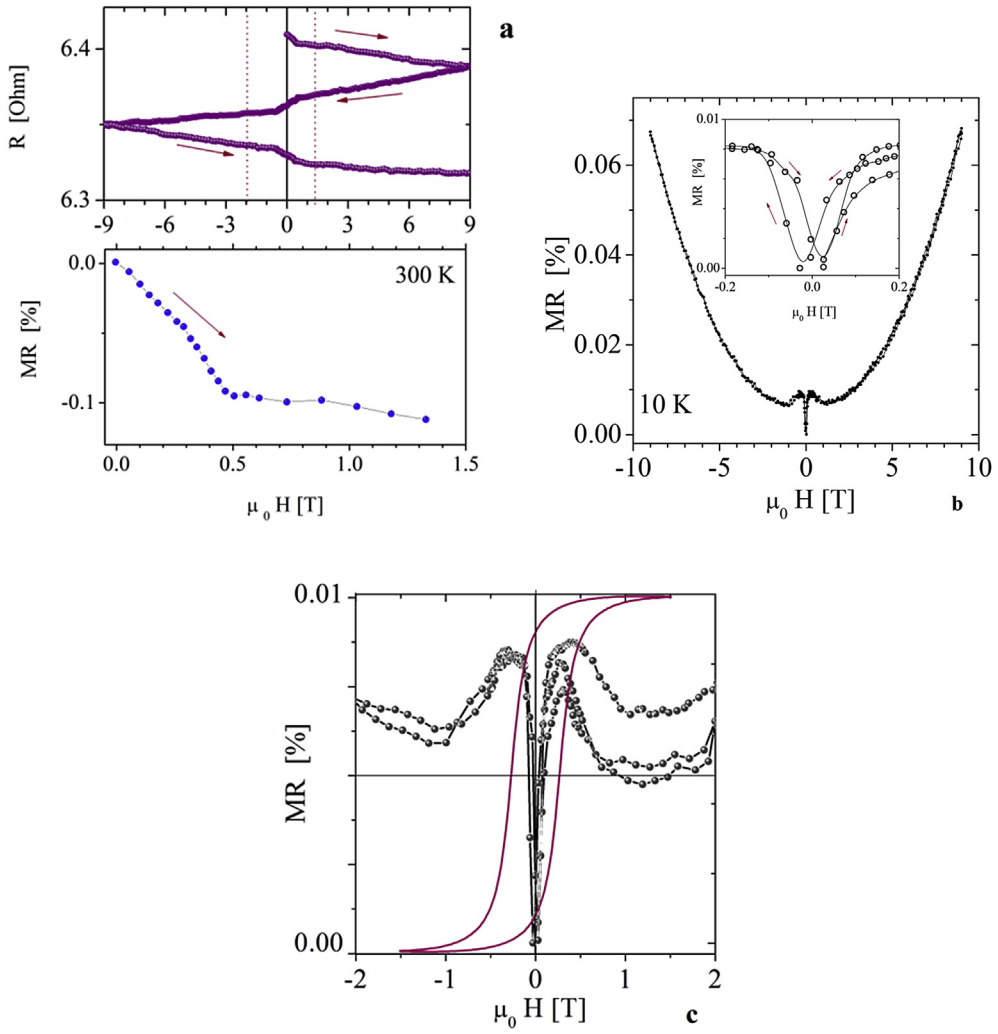

Fig. 11. Longitudinal magnetoresistance in $Fe_{90}Rh_{10}$ arrays at (a) 300 K and (b) 10 K. The inset in (b) illustrates details of the low field curve with evident hysteresis and (c) depicts the relationship between the magnetization process and magnetoresistance.

A similar low field behavior, has been reported by Ref. [40] at 4.2 K, for magnetoresistance in iron wires with intermediate diameter of ~250 nm wide and 60 μm long, epitaxially deposited onto a GaAs (110) template. Such a behavior was not observed for larger diameters.

4. Summary

Bimetallic nanowires of nominal composition $Fe_{90}Rh_{10}$, 20 nm in diameter and about 1–3 μm long, are AC electrodeposited into the cylindrical pores of AAO templates. As deposited nanowires are biphasic polycrystals, with large α-Fe grains (~150 nm long and ~20 nm diameter) and between them, agglomerates of quite small (~1.7 nm) grains of the ClCs-type α′- $Fe_{42}Rh_{58}$ phase are observed. Because of the nanowire large aspect ratio and the quite irregular (branched) shape they have an enhanced volume to surface ratio.

The easy magnetization axis of the arrays is parallel to the wire length as expected for a dominant contribution of shape effects to the effective uniaxial anisotropy in the system; this fact also explains the lower coercivity measured in Rh containing arrays.

The angular and temperature dependences of coercivity in both Fe and $Fe_{90}Rh_{10}$ nanowires are consistent with a magnetic polarization reversal mechanism controlled by the nucleation of inverse domains by local curling. The apparent activation energy at zero fields is larger in Rh containing wires, while the critical field for nucleation at 0 K is lower.

Between 4 K and 300 K, electric resistance in both arrays increases with temperature following a metallic-like behavior; at low temperature, the curves for Fe and $Fe_{90}Rh_{10}$ nanowires deviate from the Matthiessen's rule, going through a shallow minimum at about 14 K.

In $Fe_{90}Rh_{10}$ arrays, longitudinal magnetoresistance at room temperature is negative, exhibits hysteresis in the low field region and it displays a continuous drift. At low temperature this drift is absent and at high field a reversible, nearly parabolic behavior of the magnetoresistance is observed, corresponding to Lorentz magnetoresistance. Hysteresis is also observed at low fields for values below coercivity; in this range, magnetoresistance is sequentially negative, positive and again negative corresponding to AMR, electronic scattering by domain wall formation and displacement, and AMR again, respectively.

Acknowledgements

The authors wish to thank SECyT-UNC, Mincyt-Córdoba and CONICET Argentina for the financial support given to this work. The

authors are grateful to Professor Jorge L. Pelegrina for his help in sample characterization.

References

[1] R.W. Sibin Duan, Bimetallic nanostructures with magnetic and noble metals and their physicochemical applications, Prog. Nat. Sci. Mater. Int. 23 (2013) 113–126.

[2] T. Hyeon, Chemical synthesis of magnetic nanoparticles, Chem. Commun. 8 (2003) 927–934.

[3] K.M. Kang, K.M. Kim, I.W. Shim, H.Y. Kwak, Catalytic test of supported Ni catalysts with core/shell structure for dry reforming of methane, Fuel Process. Technol. 92 (2011) 1236–1243.

[4] N. Semagina, L. Kiwi-Minsker, Recent advances in the liquid- phase synthesis of metal nanostructures with controlled shape and size for catalysis, Catal. Rev Sci Eng. 51 (2009) 147–217.

[5] R. Sardar, A.M. Funston, P. Mulvaney, R.W. Murray, Gold nanoparticles: past, present, and future, Langmuir 24 (2009) 13840–13851.

[6] M. Shokouhimehr, Magnetically separable and sustainable nanostructured catalysts for heterogeneous reduction of nitroaromatics, Catalysts 5 (2015) 534–560.

[7] R.T. Mu, Q.A. Fu, H. Xu, H.I. Zhang, Y.Y. Huang, Z. Jiang, S.O. Zhang, D.L. Tan, X.H. Bao, Synergetic effect of surface and subsurface ni species at Pt–Ni bimetallic catalysts for CO oxidation, J. Am. Chem. Soc. 113 (2011) 1978–1986.

[8] D. Kodama, K. Shinoda, K. Sato, Y. Konno, R.J. Joseyphus, K. Motomiya, H. Takahash, T. Matsumoto, Y. Sato, K. Tohji, B. Jeyadevan, Chemical synthesis of sub-micrometer- to nanometer-sized magnetic FeCo dice, Adv. Mater. 18 (2006) 3154–3159.

[9] M.N. Nadagouda, R.S. Varma, A greener synthesis of core (Fe, Cu)–shell (An, Pt, Pd, and Ag) nanocrystals using aqueous vitamin C, Cryst. Growth Des. 7 (2007) 2582–2587.

[10] M. Mannin, F. Pineider, Sainctavit, C. Danieli, E. Otero, C. Sciancalepore, A.M. Talarico, M.A. Arrio, A. Cornia, D. Gatteschi, R. Sessoli, Magnetic memory of a single- molecule quantum magnet wired to a gold surface, Nat. Mater. 8 (2009) 194–197.

[11] F. Tao, M.E. Grass, Y.W. Zhang, D.R. Butcher, J.R. Renzas, Z. Liu, J.Y. Chung, B.S. Mun, M. Salmeron, G.A. Somorja, Reaction-driven restructuring of Rh–Pd and Pt–Pd core–shell nanoparticles, Science 322 (2008) 932–934.

[12] D. Fox, R. Verre, B.J. O'dowd, S.K. Arora, C.C. Faulkner, I.V. Shvets, H. Zhang, Investigation of coupled cobalt–silver nano- particle system by plan view TEM, Prog. Nat. Sci. Mater. Int. 22 (2013) 186–192.

[13] Y.H. Huang, H. Okumura, G.C. Hadjipanayis, D. Weller, CoPt and FePt nanowires by electrodeposition, J. Appl. Phys. 91 (2002) 6869.

[14] M.S. Viqueira, N. Bajales, S.E. Urreta, P.G. Bercoff, Magnetization mechanisms in ordered arrays of polycrystalline $Fe_{100-x}Co_x$ nanowires, J. Appl. Phys. 117 (2015) 204302.

[15] J. Alonso, H. Khurshid, V. Sankar, Z. Nemati, M.H. Phan, E. Garayo, J.A. García, H. Srikanth, FeCo nanowires with enhanced heating powers and controllable dimensions for magnetic hyperthermia, J. Appl. Phys. 117 (2015) 17D113.

[16] M.S. Viqueira, G. Pozo-López, S.E. Urreta, A.M. Condó, D.R. Cornejo, L.M. Fabietti, Cooperative nucleation modes in polycrystalline Co_xPd_{1-x} nanowires, J. Appl. Phys. 117 (2015) 204301–204309.

[17] M.S. Viqueira, G. Pozo-López, S.E. Urreta, A.M. Condó, D.R. Cornejo, L.M. Fabietti, Magnetic hysteresis in ordered arrays of small-grained Co_xPd_{1-x} nanowires, J. Magn. Magn. Mater. 94 (2015) 185–194.

[18] M.S. Viqueira, S.E. García, S.E. Urreta, G. Pozo-López, L.M. Fabietti, Hysteresis properties of hexagonal arrays of FePd nanowires, IEEE Trans. Magn. 49 (no. 8) (2013) 4498–4501.

[19] H. Masuda, K.S. Fakuda, Ordered metal nanohole arrays made by a two-step replication of honeycomb structures of anodic alumina, Science 268 (1995) 1466–1468.

[20] K. Nielsh, J. Choi, K. Schwirn, R.B. Wehrspohn, U. Gosele, Self-ordering regimes of porous alumina: the 10% porosity rule, Nano Lett. 2 (2002) 677–680.

[21] L.J. Swartzendruber, ASM Handbook Volume 3: Alloy Phase Diagrams, v.3, 1998, p. 853. ISBN 0-87170-381-5.

[22] J. Van Driel, R. Coehoorn, G.J. Strijkers, E. Bruk, F.R. Boer, Compositional dependence of the giant magnetoresistance in Fe_xRh_{1-x} thin films, J. Appl. Phys. 85 (1999) 1026.

[23] P. Landeros, J. Escrig, D. Altbir, D. Laroze, J. d'Albuquerque, E. Castro, P. Vargas, Scaling relations for magnetic nanoparticles, Phys. Rev. B 71 (2005) 094435.

[24] H. Kronmüller, K.D. Durst, M. Sagawa, Analysis of the *magnetic* hardening mechanism in RE-FeB permanent magnets, J. Magn. Magn. Mater. 74 (1988) 291.

[25] D. Givord, M.E. Rossignol, D.W. Taylo, Coercivity mechanisms in hard magnetic materials, Phys. IV Colloq. C3 Suppl. Phys. 111 (1992) 95.

[26] A. Aharoni, Angular dependence of nucleation by curling in a prolate spheroid, J. Appl. Phys. 82 (1997) 1281.

[27] A. Aharoni, S. Shtrikman, Magnetization curve of the infinite cylinder, Phys. Rev. 109 (1958) 1522.

[28] S. Chikazumi, Mechanism of high coercivity in rare-earth permanent magnets, J. Magn. Magn. Mater. 1 (551) (1986) 54–57.

[29] P.M. Paulus, F. Luis, M. Kröll, G. Schmid, L.J. de Jongh, Low-temperature study of the mgnetization reversal and magnetic anisotropy of Fe, Ni, and Co nanowires, J. Magn. Magn. Mater. 224 (2001) 180–196.

[30] A. Hillion, A. Cavallin, S. Vlaic, A. Tamion, F. Tournus, G. Khadra, J. Dreiser, C. Piamonteze, S. Nolting, S. Rusponi, K. Sato, T.J. Konno, O. Proux, V. Dupuis, H. Brune, Low temperature ferromagnetism in chemically ordered FeRh nanocrystals, Phys. Rev. Lett. 110 (2013) 0872071–0872075.

[31] R.B. Ross, Metallic Materials Specification Handbook, 4 Ed., Springer Science & Business Media, UK, 2013, p. 181.

[32] J. Koshy, The resistivity and temperature coefficient of resistivity of polycrystalline rhodium thin films, J. Phys. D. Appl. Phys. 13 (1980) 1339–1342.

[33] A. Mobius, F. Goedsche, D. Elefant, K.H. Berthe, Deviations from Matthiessen's rule in the low-temperature resistivity of iron, Phys. Stat. Sol. b 95 (1970) 203.

[34] O. Stierstadt, Electrical resistance of nickel and iron wires as affected by longitudinal magnetic fields, Phys. Rev. 37 (1931) 1356–1366.

[35] G.R. Taylor, A. Isin, R.V. Coleman, Resistivity of iron as a function of temperature and magnetization, Phys. Rev. 165 (1968) 621–631.

[36] A. Isin, R.V. Coleman, Dependence of magnetoresistance in iron, Phys. Rev. 142 (1966) 372–378.

[37] T. Fuji, Negative magnetoresistance effect of iron with variying impurity contents, Trans. JIM 11 (1970) 8–11.

[38] S. Takaki, K. Igaki, Electrical resistivity of high-purity iron at 4.2 K, Trans. JIM 17 (1976) 353–359.

[39] P.N. Dheer, Galvanomagnetic effects in iron whiskers, Phys. Rev. 156 (1967) 637–644.

[40] C. Hassel, F.M. Römer, R. Meckenstock, G. Dumpich, Magnetization reversal in epitaxial Fe nanowires on GaAs(110), Phys. Rev. B 77 (2008) 224439.